



**HAL**  
open science

## Chemical bonding in $RFe_6Ge_4$ ( $R = Li, Sc, Zr$ ) and $LuTi_6Sn_4$ with rhombohedral $LiFe_6Ge_4$ type structure

Samir F. Matar, Thomas Fickenscher, Birgit Gerke, Oliver Niehaus, Ute Ch. Rodewald, Adel F. Al Alam, Naïm Ouaini, Rainer Pöttgen

► **To cite this version:**

Samir F. Matar, Thomas Fickenscher, Birgit Gerke, Oliver Niehaus, Ute Ch. Rodewald, et al.. Chemical bonding in  $RFe_6Ge_4$  ( $R = Li, Sc, Zr$ ) and  $LuTi_6Sn_4$  with rhombohedral  $LiFe_6Ge_4$  type structure. Solid State Sciences, 2015, 39, pp.82-91. 10.1016/j.solidstatesciences.2014.11.011 . hal-01110912

**HAL Id: hal-01110912**

**<https://hal.science/hal-01110912>**

Submitted on 29 Jan 2015

**HAL** is a multi-disciplinary open access archive for the deposit and dissemination of scientific research documents, whether they are published or not. The documents may come from teaching and research institutions in France or abroad, or from public or private research centers.

L'archive ouverte pluridisciplinaire **HAL**, est destinée au dépôt et à la diffusion de documents scientifiques de niveau recherche, publiés ou non, émanant des établissements d'enseignement et de recherche français ou étrangers, des laboratoires publics ou privés.

## Chemical bonding in $R\text{Fe}_6\text{Ge}_4$ ( $R = \text{Li}, \text{Sc}, \text{Zr}$ ) and $\text{LuTi}_6\text{Sn}_4$ with rhombohedral $\text{LiFe}_6\text{Ge}_4$ type structure

Samir F. Matar<sup>a</sup>, Thomas Fickenscher<sup>b</sup>, Birgit Gerke<sup>b</sup>, Oliver Niehaus<sup>b</sup>, Ute Ch. Rodewald<sup>b</sup>, Adel F. Al Alam<sup>c</sup>, Naïm Ouaini<sup>c</sup>, Rainer Pöttgen<sup>b,\*</sup>

<sup>a</sup> CNRS, Université de Bordeaux, ICMCB, 33600 Pessac, France

<sup>b</sup> Institut für Anorganische und Analytische Chemie, Universität Münster, Corrensstrasse 30, D-48149 Münster, Germany

<sup>c</sup> Holy Spirit University-USEK, OCM, CSR-USEK, CNRS\_L, Jounieh, Lebanon

\* Correspondence and reprints: Institut für Anorganische und Analytische Chemie, Westfälische Wilhelms-Universität Münster, Corrensstrasse 30, 48149 Münster, Germany, Tel.: +49-251-83-36001; Fax: +49-251-83-36002

*E-mail addresses:* pottgen@uni-muenster.de (R. Pöttgen), matar@icmcb-bordeaux.cnrs.fr (S. F. Matar)

---

### ARTICLE INFO

---

*Article history:*

---

*Keywords:*

Germanides

Stannides

Kagomé network

Chemical bonding

---

### ABSTRACT

---

The germanide  $\text{ScFe}_6\text{Ge}_4$  was synthesized from the elements by arc-melting. Its crystal structure was refined from single crystal X-ray diffractometer data:  $\text{LiFe}_6\text{Ge}_4$  type,  $R\bar{3}m$ ,  $a = 507.9(3)$ ,  $c = 2000.9(1)$  pm,  $wR2 = 0.0737$ , 242  $F^2$  values, 16 variables. The structure has two main building units. The iron atoms form double-layers of Kagomé networks (248-297 pm Fe–Fe) which are separated by layers of edge-sharing Sc@Ge<sub>8</sub>

hexagonal bipyramids (265-293 pm Sc–Ge). Chemical bonding has been studied based on DFT calculations for the  $A\text{Fe}_6\text{Ge}_4$  ( $A = \text{Li}, \text{Sc}, \text{Zr}$ ) series and isotypic  $\text{LuTi}_6\text{Sn}_4$ . Existence of  $\text{MgFe}_6\text{Ge}_4$  is proposed on the basis of full geometry optimization. Major differences are observed between the electronic structures and the magnetic properties and bonding of  $\text{LuTi}_6\text{Sn}_4$  on the one hand and the  $A\text{Fe}_6\text{Ge}_4$  family on the other hand whereby the iron Kagomé substructure develops magnetization in all  $A\text{Fe}_6\text{Ge}_4$  compounds, in contrast to  $\text{LuTi}_6\text{Sn}_4$ . The Ti–Ti Kagomé substructure is found with bonding character throughout the valence band whereas Fe–Fe interactions are both bonding and antibonding with characteristic spin-dependent bonding. Spin-polarized calculations hint for magnetic ordering in the iron containing representatives. This was proven experimentally for  $\text{ScFe}_6\text{Ge}_4$ . Temperature-dependent susceptibility measurements show a Curie temperature of  $T_C = 491(3)$  K.  $^{57}\text{Fe}$  Mössbauer spectroscopic measurements at ambient temperature show a single resonance at an isomer shift of  $0.22(1)$   $\text{mm}\cdot\text{s}^{-1}$  with a magnetic hyperfine field of  $19.1(1)$  T.

© 2014 Elsevier Masson SAS. All rights reserved.

---

## 1. Introduction

Kagomé networks of transition metal atoms are important basic building units in diverse intermetallic structure types. Prominent examples are the hexagonal Laves phases [1, 2] and the huge family of  $\text{CaCu}_5$  phases [3, 4] and related superstructures [5]. Such triangular systems are interesting model compounds for the study of frustration, especially for magnetically ordering phases [6].

Stacking of Kagomé networks has also been observed in the rare structure type  $\text{LiFe}_6\text{Ge}_4$  [7, 8]. The few representatives are listed in Table 1. The transition metal atoms form the Kagomé networks and they are separated by hexagonal bipyramids of tetrel atoms around the cations (Li, Sc, Zr, or a rare earth element). So far only few studies on magnetic properties have been reported for the  $RE\text{Ti}_6\text{Sn}_4$  series ( $RE = \text{Gd-Tm}$ ) [12]. These compounds are paramagnets down to 3 K.

The family of  $\text{LiFe}_6\text{Ge}_4$  type compounds is well suited for a systematic study of chemical bonding as a function of the cation and the valence electron count per formula

unit, similar to the series of  $\text{LiCo}_6\text{P}_4$  [16] and  $\text{U}_4\text{Re}_7\text{Si}_6$  type compounds [17]. Herein we report on single crystal X-ray diffraction data of  $\text{ScFe}_6\text{Ge}_4$  (so far only powder X-ray diffraction data were reported [9, 10]) and a comparative study of the chemical bonding of  $R\text{Fe}_6\text{Ge}_4$  ( $R = \text{Li}, \text{Sc}, \text{Zr}$ ) and  $\text{LuTi}_6\text{Sn}_4$  [12] with the remarkable motif of titanium Kagomé networks.

## 2. Experimental

### 2.1. Synthesis

Starting materials for the preparation of the  $\text{ScFe}_6\text{Ge}_4$  sample were pieces of scandium chips (Smart Elements), iron granules (Alfa Aesar) and germanium granules (Chempur), all with stated purities  $> 99.9\%$ . Pieces of the three elements were mixed in the ideal 1 : 6 : 4 atomic ratio and arc-melted [18] under an argon pressure of ca. 800 mbar. The argon was purified over titanium sponge (900 K), silica gel and molecular sieves. The product button was re-melted several times to ensure homogeneity. The total weight-loss after several meltings was smaller than 0.5 %. The brittle  $\text{ScFe}_6\text{Ge}_4$  sample has metallic luster and is stable in air over weeks.

The arc-melted sample was essentially polycrystalline. For the growth of small single crystals for structure refinement, a small piece of polycrystalline  $\text{ScFe}_6\text{Ge}_4$  was sealed in an evacuated silica tube and annealed in a muffle furnace at 970 K for three weeks.

### 2.1. EDX data

Semiquantitative EDX analyses of the  $\text{ScFe}_6\text{Ge}_4$  crystals investigated on the diffractometer were carried out by use of a Zeiss EVO<sup>®</sup> MA10 scanning electron microscope in variable pressure mode with scandium, iron and germanium as standards. The experimentally observed composition of  $10 \pm 1$  at.-% Sc :  $56 \pm 1$  at.-% Fe :  $34 \pm 1$  at.-% Ge was close to the ideal one (9.1 : 54.5 : 36.4). No impurity elements were observed.

### 2.2. X-Ray diffraction

The  $\text{ScFe}_6\text{Ge}_4$  sample was characterized through a Guinier powder diffractogram using  $\text{CuK}_{\alpha 1}$  radiation and  $\alpha$ -quartz ( $a = 491.30$  and  $c = 540.46$  pm) as an internal standard. The Guinier camera was equipped with an imaging plate technique (Fuji Film, BAS-READER 1800). The lattice parameters (Table 1) were obtained from a least-

squares refinement. The experimental pattern was compared to a calculated one [19] to ensure correct indexing.

Small single crystals of  $\text{ScFe}_6\text{Ge}_4$  were isolated from the crushed annealed sample. They were glued to thin quartz fibers and investigated on a Buerger precession camera (white Mo radiation, Fuji-film imaging plate) in order to check their quality for intensity data collection. The data set was collected at room temperature by using a STADIVARI (Mo microfocus source and a Pilatus 100 K Detector with a hybrid-pixel-sensor) diffractometer. A spherical absorption correction was applied to the data set. Details on the crystallographic data are given in Table 2.

### 2.3. Computational details

An appropriate framework for the study of the electronic structure and the qualitative bonding behavior is the quantum density functional theory DFT [20, 21]. Among the many computational methods built within the DFT we used two of them in a complementary manner. The Vienna *ab initio* simulation package (VASP) code [22-24] allows geometry optimization and cohesive energy calculations; it was also used to predict the electronic properties of  $\text{MgFe}_6\text{Ge}_4$  starting from those determined herein for  $\text{ScFe}_6\text{Ge}_4$ . For this we used the projector augmented wave (PAW) method [23, 25], with the generalized gradient approximation (GGA) scheme following Perdew, Burke and Ernzerhof (PBE) [26]. For Li, Mg, Sc and Zr the semi-core states were included for the building of the potentials. This enables for a better chemical picture in the solid state, ex. Li with 3 electrons ( $1s^2, 2s^1$ ), i.e. with a larger basis including core electrons, provides a charge of  $\text{Li}^{+0.82}$  in  $\text{LiFe}_6\text{Ge}_4$  instead of fully ionized  $\text{Li}^{+1}$  if only  $2s^1$  were considered (cf. section 3.3.1). In fact the larger the basis set the better the results so that one avoids excessively ionic behavior far from reality. For instance this is the case of the ionic metal hydride  $\text{MgH}_2$  where, if Mg  $3s^2$  states are only considered, then we have  $\text{Mg}^{2+}$ ,  $\text{H}^{-1}$  from the calculations, which doesn't reproduce reality. Including semi-core Mg  $2p^6$  in the construction of the pseudo-potentials is then needed to get  $\text{H}^{-0.82}$ , closer to reality. Preliminary calculations with local density approximation LDA [27] led to largely underestimated volumes versus the experiment; the LDA being known as over-binding. The conjugate-gradient algorithm [28] is used in this computational scheme to relax the atoms. The tetrahedron method with Blöchl corrections [29] as well as a Methfessel-Paxton [30] scheme was applied for both geometry relaxation and total

energy calculations. Brillouin-zone (BZ) integrals were approximated using the special k-point sampling. The optimization of the structural parameters was performed until the forces on the atoms were less than  $0.02 \text{ eV/\AA}$  and all stress components less than  $0.003 \text{ eV/\AA}^3$ . The calculations are converged at an energy cut-off of 500 eV for the plane-wave basis set with respect to the k-point integration up to  $11 \times 11 \times 11$  ( $k_x, k_y, k_z$ ) for best convergence and relaxation to zero strains. The calculations are scalar relativistic and assume spin degenerate total spins. Then all-electron calculations with the GGA were carried out for a full description of the electronic structure and the chemical bonding, using the augmented spherical wave (ASW) method devised by Williams, Kübler and Gelatt in 1979 [31] as a linearized method close to the LMTO (Linearized Muffin Tin Orbitals) method. It has benefited from continuous developments leading to full potential FP-ASW with implementation of chemical bonding according to different schemes (cf. text book by V. Eyert [32] and therein references). The ASW method uses a minimal basis set for the valence states with the outermost shells representing one of each kind: the valence states and the matrix elements are constructed using partial waves up to  $l_{\max}+1 = 4$  for Lu,  $l_{\max}+1 = 3$  for Fe, Sc and Zr and  $l_{\max}+1 = 2$  for Li, Mg and Ge. Self-consistency is achieved when charge transfers and energy changes between two successive cycles were below  $10^{-8}$  and  $10^{-6}$  eV, respectively. BZ integrations were performed using the linear tetrahedron method within the irreducible wedge. Besides the site projected density of states, we discuss qualitatively the pair interactions based on the overlap population analysis with the crystal orbital overlap population (COOP) [33]. In the plots, positive, negative, and zero COOP indicate bonding, anti-bonding, and non-bonding interactions, respectively.

#### *2.4. Magnetic susceptibility measurements*

The magnetic measurements were carried out on a Quantum Design Physical Property Measurement System (PPMS) using the VSM (Vibrating Sample Magnetometer) and the VSM-Oven option. In order to achieve temperatures above 350 K the latter one is equipped with a heater stick, additionally. For the VSM measurement in the low-temperature area a 15.661 mg piece of the crushed sample was fixed to the sample holder rod, while a 15.316 mg piece was attached to the heater stick by using an alumina based cement. For all measurements above 300 K, the sample was at first heated up to 600 K to ensure a virgin sample. Due to the heating limits of the low-

temperature option [ $T_{\max}$  (VSM)  $\approx$  400 K] this is not accessible with our equipment. Magnetic investigations were performed in the temperature range of 3 to 600 K with magnetic flux densities up to 80 kOe.

### 2.5. $^{57}\text{Fe}$ Mössbauer spectroscopy

A  $^{57}\text{Co/Rh}$  source was available for the  $^{57}\text{Fe}$  Mössbauer spectroscopic investigations. 40 mg of  $\text{ScFe}_6\text{Ge}_4$  were placed in a thin-walled PVC container at an optimized thickness of about 6.4 mg Fe/cm<sup>2</sup>. The measurements were performed by using the usual transmission geometry at ambient temperature. The spectrum was fitted by using the Normos-90 program system [34].

## 3. Results and discussions

### 3.1. Structure refinement

The  $\text{ScFe}_6\text{Ge}_4$  data set showed a trigonal lattice and no further systematic extinctions. The centrosymmetric space group  $R\bar{3}m$  was found to be correct in agreement with previous studies on the stannides  $RE\text{Ti}_6\text{Sn}_4$  [12]. The atomic positions of  $\text{LuTi}_6\text{Sn}_4$  [12] were taken as starting values and the structure was refined with anisotropic displacement parameters for all atoms with Shelxl-97 (full-matrix least-squares on  $F_o^2$ ) [35]. In order to check for deviations from the ideal composition, the occupancy parameters were refined in separate series of least-squares cycles. All sites were fully occupied within three standard deviations. The final difference Fourier synthesis revealed no significant residual densities. The atomic coordinates and interatomic distances are listed in Tables 3 and 4.

Further details of the structure refinement may be obtained from the Fachinformationszentrum Karlsruhe, D-76344 Eggenstein-Leopoldshafen (Germany), by quoting the Registry No. CSD-428504.

### 3.2. Crystal Chemistry

A view of the  $\text{ScFe}_6\text{Ge}_4$  structure approximately along the [110] direction is presented in Fig. 1, emphasizing the Kagomé networks formed by the iron atoms as well as the  $\text{Sc@Ge}_8$  hexagonal bipyramids. The Fe–Fe distances within the Kagomé networks of 248 and 260 pm are slightly longer than twice the covalent radius of 232 pm [36], but close to the Fe–Fe distance of 248 pm in *bcc* iron [37], indicating substantial Fe–Fe bonding interactions.

The Kagomé networks are stacked in AABBC sequence. Each pair of Kagomé networks forms a kind of sandwich for the Sc@Ge<sub>8</sub> hexagonal bipyramids. The apices of the bipyramids penetrate the hexagons of the Kagomé networks. The Sc@Ge<sub>8</sub> hexagonal bipyramids share six common edges in the *ab* plane. Although this is a purely geometrical description of the ScFe<sub>6</sub>Ge<sub>4</sub> structure, it allows a complete description with only two basic building units.

The Sc–Ge bond lengths within the Sc@Ge<sub>8</sub> hexagonal bipyramids cover a broader range. The two apices are at the shorter Sc–Ge distances of 265 pm, close to the sum of the covalent radii of 266 pm [36]. The six germanium atoms building the ground plane of the bipyramid are at the much longer distance of 293 pm, indicating an asymmetrical bonding pattern.

Both of the two crystallographically independent germanium sites have nine, respectively six nearest iron neighbors with Fe–Ge distances ranging from 249 to 261 pm, similar to the binary iron germanides FeGe<sub>2</sub> (254 pm) [38] and Fe<sub>6</sub>Ge<sub>5</sub> (238–270) [39]. These Fe–Ge bonds interconnect the Kagomé networks and the Sc@Ge<sub>8</sub> hexagonal bipyramids.

These ternary iron germanides exist with lithium, scandium, and zirconium at the 3*a* Wyckoff site. In going from the lithium to the zirconium representative, one observes an increase of the *a* and *c* lattice parameters (Table 1), a consequence of the different covalent radii of 123, 144, and 145 pm for lithium, scandium, and zirconium, respectively. This difference in size mainly influences the bonding to the two shorter Li–Ge, Sc–Ge, and Zr–Ge neighbors. The influence of the different valence electron count (65, 67, and 68 for LiFe<sub>6</sub>Ge<sub>4</sub>, ScFe<sub>6</sub>Ge<sub>4</sub>, and ZrFe<sub>6</sub>Ge<sub>4</sub>, respectively) is discussed below on the basis of *ab initio* electronic structure calculations. Keeping the size and the diagonal relationship between lithium and magnesium (covalent radius of 136 pm) in mind, one might also speculate about a magnesium-containing representative. However, so far, our synthesis efforts gave no hint for such a compound.

Apart from the germanides the isostructural series of *RE*Ti<sub>6</sub>Sn<sub>4</sub> stannides exists [12–15]. The much larger tin atoms along with the rare earth atoms force a drastic increase of the *a* and *c* lattice parameters (Table 1). These stannides contain the remarkable motif



of a titanium Kagomé network with a distinctly lower valence electron count of 43. In the following section we evaluate the electronic structures of the germanides  $\text{LiFe}_6\text{Ge}_4$ ,  $\text{ScFe}_6\text{Ge}_4$ , and  $\text{ZrFe}_6\text{Ge}_4$  along with the stannide  $\text{LuTi}_6\text{Sn}_4$ .

### 3.3. Electronic structure and chemical bonding

#### 3.3.1. Geometry optimization, cohesive energies and relative charge transfer

From Table 5 the geometry optimized crystal structure results of  $\text{ScFe}_6\text{Ge}_4$  are found in relatively good agreement with the experiment. The results were then used to predict the values for the as yet non-synthesized germanide  $\text{MgFe}_6\text{Ge}_4$ . This helps drawing trends of cohesive energies in the  $A\text{Fe}_6\text{Ge}_4$  ( $A = \text{Li}, \text{Mg}, \text{Sc}$  and  $\text{Zr}$ ) series. The cohesive energies can be obtained from the difference between the total energy at self consistent convergence on the one hand and those of the atomic constituents in their ground state structures on the other hand:

$$E(\text{LiFe}_6\text{Ge}_4) = -69.83 \text{ eV/cell}; E(\text{MgFe}_6\text{Ge}_4) = -68.63 \text{ eV/cell}; E(\text{ScFe}_6\text{Ge}_4) = -75.11 \text{ eV/cell}; E(\text{ZrFe}_6\text{Ge}_4) = -76.93 \text{ eV/cell}.$$

$$E(\text{Li}) = -1.92 \text{ eV/at.}; E(\text{Mg}) = -1.39 \text{ eV/at.}; E(\text{Sc}) = -6.18 \text{ eV/at.}; E(\text{Zr}) = -8.53 \text{ eV/at.}; E(\text{Fe}) = -7.82 \text{ eV/at.}; E(\text{Ge}) = -4.48 \text{ eV/at.}.$$

The resulting cohesive energies are then:

$$E_{coh.}(\text{LiFe}_6\text{Ge}_4) = -3.07 \text{ eV/cell}; E_{coh.}(\text{MgFe}_6\text{Ge}_4) = -2.40 \text{ eV/cell}; E_{coh.}(\text{ScFe}_6\text{Ge}_4) = -4.09 \text{ eV/cell}; E_{coh.}(\text{ZrFe}_6\text{Ge}_4) = -3.56 \text{ eV/cell}.$$

The negative values for all four ternaries point to cohesive compounds. Particularly the hypothetical  $\text{MgFe}_6\text{Ge}_4$  should be able of synthesis. However the trends of cohesive energies are not homogeneously changing along the series, i.e. with the regular increase of the number of electrons from  $A = \text{Li}, \text{Mg}, \text{Sc}$  and  $\text{Zr}$  one can notice that the most stable compound is  $\text{ScFe}_6\text{Ge}_4$ . Regarding  $\text{LuTi}_6\text{Sn}_4$ , the cohesive energy is large and amounts to  $-4.76 \text{ eV/cell}$  leading to assign it the largest stability.

Electron transfer via charge values are obtained from the analysis of the charge density CHGCAR issued from VASP calculations using the AIM (atoms in molecules theory) approach [40]. Typically in a heteroatomic chemical bond, the charge density reaches a minimum between atoms and this is a natural region to separate them from each other. Such an analysis does not constitute a tool for evaluating absolute

ionizations but allows establishing trends between similar chemical compounds. For the compounds under consideration the average charge values ( $Q$ ) are:

$$\text{LiFe}_6\text{Ge}_4: Q(\text{Li}) = +0.82; Q(\text{Fe}) = -0.03; Q(\text{Ge}) = -0.16$$

$$\text{MgFe}_6\text{Ge}_4: Q(\text{Mg}) = +1.66; Q(\text{Fe}) = -0.05; Q(\text{Ge}) = -0.34$$

$$\text{ScFe}_6\text{Ge}_4: Q(\text{Sc}) = +1.42; Q(\text{Fe}) = -0.07; Q(\text{Ge}) = -0.25$$

$$\text{ZrFe}_6\text{Ge}_4: Q(\text{Zr}) = +1.34; Q(\text{Fe}) = -0.05; Q(\text{Ge}) = -0.26$$

In all four compounds Fe keeps a metallic behavior with very small negative magnitude of charge whereas the electron transfer is mainly within the  $A@Ge_8$  entities. Whereas monovalent Li shows the expected charge transfer magnitude, close but smaller than 1 as discussed in the computational details above, one should notice the large magnitude of electron transfer from Mg to Ge in hypothetical  $\text{MgFe}_6\text{Ge}_4$  contrary to the Sc and Zr compounds. Also it can be noted that the charge transfer trends do not follow the course of the electronegativity values:  $\chi(\text{Li}) = 0.98$ ,  $\chi(\text{Mg}) = 1.31$ ,  $\chi(\text{Sc}) = 1.36$ ;  $\chi(\text{Zr}) = 1.33$ ;  $\chi(\text{Fe}) = 1.83$  and  $\chi(\text{Ge}) = 2.01$ . This could be assigned to the particular feature of the Kagomé Fe substructure between the  $A@Ge_8$  units. Particularly the divalent, trivalent and tetravalent characters of Mg, Sc and Zr, respectively, do not appear as it would show in more ionic compounds as oxides for instance; this is also valid for the most electronegative element of the series, Ge, and most likely arises from the covalent bonding character.

Different charge transfers are observed for  $\text{LuTi}_6\text{Sn}_4$  with  $Q(\text{Lu}) = +1.36$ ;  $Q(\text{Ti}) = +1.14$  and  $Q(\text{Sn}) = -2.05$ . This is likely connected with the more electropositive character of titanium as compared to iron (see the course of the electronegativities  $\chi(\text{Ti}) = 1.54$  and  $\chi(\text{Fe}) = 1.83$ ).

### 3.3.2 All-electron calculations and bonding properties

Using the experimental data of Tables 1 and 2 we carried out detailed calculations of the electronic structure and chemical bonding with the scalar relativistic ASW method. The calculations assume firstly non-spin-polarized (NSP) configurations. At self consistent convergence of the energies and charges, small charge transfers similar to the above trends were obtained. The site projected density of states PDOS are shown in Fig.

2. The energy reference along the  $x$  axis is with respect to the Fermi level  $E_F$ . For the sake of completeness the DOS of hypothetical  $MgFe_6Ge_4$  are included.

$LuTi_6Sn_4$  (Fig. 2 a) shows different features from the  $AFe_6Ge_4$  series (Figs. 2 b-e). This is particularly exhibited by strongly localized Lu  $4f$  within the valence band (VB) at  $\sim -5$  eV due to their filling up to saturation with 14 electrons on the one hand and with the broader Ti PDOS versus Fe PDOS which cross the Fermi level at much higher magnitude on the other hand. This also arises from the low filling of the Ti  $3d$  states versus the larger filling of Fe  $3d$  states. The localization of the latter and the large Fe  $d$ -PDOS magnitude at  $E_F$  are a strong indication for a magnetic instability of the Fe compounds in the presently considered spin degenerate NSP configuration in the Stoner theory of band ferromagnetism [41]. This mean field Stoner theory can be applied to address the tendency for spin polarization. This is shortly presented: The total energy of a spin system results from the exchange and kinetic energies. Referring the total energy to the non-magnetic state, this is expressed as:  $E = constant\{1 - \mathcal{J}n(E_F)\}$ . In this expression,  $\mathcal{J}$  (eV) is the Stoner integral, which is calculated and tabulated for the metals by Janak [42] and  $n(E_F)$  (1/eV) is the PDOS value for a given state -mainly  $d$ - at the Fermi level in the non-magnetic state. If the unit-less Stoner product  $\mathcal{J}n(E_F)$  is larger than 1,  $E$  is lowered and the system stabilizes in a magnetically ordered configuration. Then the product  $\mathcal{J}n(E_F)$  provides a criterion for the stability of the spin system.

Considering the NSP results for  $LuTi_6Sn_4$  and  $AFe_6Ge_4$ , the PDOS at  $E_F$ ,  $n(E_F)$ , amount to  $n_{Ti}(E_F) = 1.69 \text{ eV}^{-1}$  on the one hand and  $n_{(E_F)LiFe_6Ge_4} = 4.5 \text{ eV}^{-1}$ ,  $n_{(E_F)ScFe_6Ge_4} = 4.8 \text{ eV}^{-1}$ ,  $n_{(E_F)MgFe_6Ge_4} = 4.9 \text{ eV}^{-1}$  and  $n_{(E_F)ZrFe_6Ge_4} = 4.7 \text{ eV}^{-1}$  on the other hand. From ref. [42] the Stoner integral values are  $\mathcal{J}\{Ti\} = 0.34 \text{ eV}$  and  $\mathcal{J}\{Fe\} = 0.46 \text{ eV}$  resulting into  $\mathcal{J}_{Fe} \cdot n_{Fe}(E_F) = 2.08, 2.26, 2.22$  and  $2.17$  for  $AFe_6Ge_4$  with  $A = Li, Mg, Sc$  and  $Zr$  respectively. On the other side  $\mathcal{J}_{Ti} \cdot n_{Ti}(E_F) = 0.58$ . Then the Stoner criterion  $1 - \mathcal{J}n(E_F)$  is negative for the  $AFe_6Ge_4$  family, not for  $LuTi_6Sn_4$ .

Energy lowering upon the onset of magnetization, *i.e.* intra-band spin-polarization should occur when spin polarization is allowed. Subsequent spin polarized (SP) calculations with equal initial  $\uparrow$  and  $\downarrow$  spin populations, were carried out. At self-consistency a finite magnetization can be identified within an implicit long range ferromagnetic order. Nevertheless if magnetic exchange energy is not sufficient, zero

local moments can result, so that the calculations are not biased initially. This also depends on the BZ mesh precision, i.e. the calculations are usually carried out in steps of increasing precision until no more changes are observed in the variational energy and the magnetic moments. Subsequent spin polarization (SP) led to a non magnetic solution for  $\text{LuTi}_6\text{Sn}_4$  (as also determined experimentally [12]) and to a large energy stabilization  $\Delta E(\text{SP-NSP}) \sim -2$  eV within the  $\text{AFe}_6\text{Ge}_4$  series thanks to magnetic exchange. This confirms the Stoner criterion trends discussed above and finite moments could be identified on Fe with small negative moments on A and Ge arising from the mixing of the valence states of the respective basis sets through the chemical bond:

$$\text{LiFe}_6\text{Ge}_4: M(\text{Li}) = -0.04 \mu_{\text{B}}; M(\text{Fe}) = 1.64 \mu_{\text{B}}; M_{\text{average}}(\text{Ge}) = -0.1 \mu_{\text{B}}.$$

$$\text{MgFe}_6\text{Ge}_4: M(\text{Mg}) = -0.04 \mu_{\text{B}}; M(\text{Fe}) = 1.79 \mu_{\text{B}}; M_{\text{average}}(\text{Ge}) = -0.1 \mu_{\text{B}}.$$

$$\text{ScFe}_6\text{Ge}_4: M(\text{Sc}) = -0.05 \mu_{\text{B}}; M(\text{Fe}) = 1.78 \mu_{\text{B}}; M_{\text{average}}(\text{Ge}) = -0.1 \mu_{\text{B}}.$$

$$\text{ZrFe}_6\text{Ge}_4: M(\text{Zr}) = -0.02 \mu_{\text{B}}; M(\text{Fe}) = 1.82 \mu_{\text{B}}; M_{\text{average}}(\text{Ge}) = -0.05 \mu_{\text{B}}.$$

The calculated SP configuration implicitly applies for a ferromagnetic ground state. Also antiferromagnetic configurations were obtained by doubling the unit cell along  $c$  and by considering Fe as UP SPINS in the first and as DOWN SPINS in the second one (AF1) on one hand and by considering Fe as half UP and half DOWN in the first subcell and half DOWN and half UP in the second cell (AF2), on the other hand. Both AF configurations led to a raise of the energy with respect to SP-Ferro configuration although with different magnitudes, i.e.  $\Delta E(\text{SP-AF1}) \sim -0.51$  eV;  $\Delta E(\text{SP-AF2}) \sim -0.22$  eV. In spite of the small energy magnitude for the latter, the results are comforted by the property studies of  $\text{ScFe}_6\text{Ge}_4$  which lead to a ferromagnetic ground state (*vide infra*).

The site and spin projected DOS are shown in Fig. 3 for all five 1:6:4 compounds. Contrary to the  $\text{AFe}_6\text{Ge}_4$  series (Fig. 3 b-e) which clearly show an energy shift between  $\uparrow$  and  $\downarrow$  spin PDOS with the former towards lower energy within the VB and the latter at higher energy whence their labeling respectively as majority and minority spins, there is no shift between  $\uparrow$  and  $\downarrow$  spin PDOS in  $\text{LuTi}_6\text{Sn}_4$ . (Fig. 3a). This reflects the magnetic results discussed above and shows that the Fermi level crosses a small magnitude Fe  $\uparrow$  PDOS and a large  $\downarrow$  spin PDOS. Then spin polarization has led to an overall lowering of

the density of states at  $E_F$  which goes along with the energy stabilization and underlines different bonding characteristics between the NSP and SP configurations.

In the NSP and SP DOS panels, the VB is characterized below  $\sim -2$  eV by the itinerant states of the respective constituents showing similar PDOS shapes. This indicates the mixing between the states accounted for in the basis set. Also within the transition metal Kagomé substructure Ti–Ti and Fe–Fe bonding is expected. These features are made explicit with the analysis of the chemical bonding using the COOP approach, exemplarily for  $\text{LuTi}_6\text{Sn}_4$  and  $\text{ScFe}_6\text{Ge}_4$ . Figs. 4 a) and b) show the interactions between elements of the same nature considering NSP configuration accounting for the different multiplicities of the Wyckoff sites, i.e. with the proportion 1:6:4. While Lu–Lu and Sc–Sc interactions are negligible as one may expect from the structural feature of their enclosing within Sn (Ge) bipyramids, the Sn–Sn and Ge–Ge COOP are half bonding (positive magnitudes) and half antibonding (negative magnitudes) so that they do not contribute to the cohesion within the structure. Different bonding features appear for Ti–Ti versus Fe–Fe: Whereas the former are of positive magnitudes, i.e. bonding, strong anti-bonding COOP appear for Fe–Fe at  $E_F$ , i.e. concomitantly with the large Fe PDOS at  $E_F$  in Figs. 2. The magnetic instability of the Fe based compounds is then mainly due to Fe–Fe anti-bonding interactions. Then it becomes relevant to examine the change of the bonding upon spin polarization. The total  $\uparrow$  and  $\downarrow$  spin COOP are shown in Fig. 4c. The relative energy shifts observed in Figs. 3 are followed in the COOP and lower magnitude antibonding COOP's are observed at  $E_F$ . The  $\uparrow$  spin COOP are mainly bonding with some anti-bonding contribution at  $\sim -2$  eV arising from Fe–Fe COOP whereas  $\downarrow$  spin COOP are all of bonding nature with very small negative COOP at the top of the VB. Bonding is then spin-dependent whereby it is larger for minority spins thus bringing stabilization to this compound.

Focusing on the interactions between chemical species within the substructures of different kinds, Fig. 5 explicates them within NSP  $\text{ScFe}_6\text{Ge}_4$ . Clearly the weakest bonding occurs between Sc and Fe which are isolated from each other by the  $\text{Sc}@Ge_8$  hexagonal bipyramids. The COOP run similarly to the DOS from the energy standpoint whereby the bonding occurs with Fe d states at (anti-bonding) and slightly below (bonding)  $E_F$ . On the opposite, Fe–Ge interactions are of bonding nature and occur at

lower energy within the VB, i.e. at the Ge  $p$ -PDOS. This is similar to the Ti–Sn interactions in LuTi<sub>6</sub>Sn<sub>4</sub> shown in panel (d) which exhibit bonding behavior throughout the VB and keep a bonding behavior a few eV above  $E_F$ . In spite of the Sc@Ge<sub>8</sub> polyhedra Sc–Ge bonding is of lower magnitude (due to the small multiplicity of 1:2 on each Ge site with slightly larger in-plane Sc–Ge<sub>2</sub> COOP magnitudes versus Sc–Ge<sub>1</sub>).

#### 3.4. Magnetic properties of ScFe<sub>6</sub>Ge<sub>4</sub>

At first the low-temperature area (3–300 K) of ScFe<sub>6</sub>Ge<sub>4</sub> was investigated by performing a ZFC (zero-field-cooled) measurement at an applied field of 10 kOe (not shown here). Due to a significant magnetic moment per formula unit and the absence of any Curie-Weiss like behavior, we decided to perform measurements above 300 K. The top panel of Fig. 6 presents the temperature dependence of the magnetic and inverse magnetic susceptibility ( $\chi$  and  $\chi^{-1}$  data) of ScFe<sub>6</sub>Ge<sub>4</sub> in the range of 300 to 600 K measured at 10 kOe. Due to limitations of our equipment we were not able to obtain reproducible results above 600 K. Within the investigated temperature area and in accordance to the theoretical calculations (*vide supra*) a ferromagnetic ordering can be clearly observed slightly below 500 K. Above the magnetic ordering an initial linear temperature dependency of the reciprocal susceptibility can be observed. Unfortunately, the linear range is not sufficient to execute a reliable fit by using the Curie-Weiss law.

In order to obtain more precise information about this cooperative phenomenon, a low-field measurement was performed in a zero-field- and field-cooled mode (ZFC/FC) which is shown in the inset of the top panel of Fig. 6. A significant bifurcation between the ZFC- and the FC-curves is visible which is typical for a ferromagnet and the Curie temperature could be determined to be  $T_C = 491(3)$  K.

The bottom panel in Fig. 6 displays the magnetization isotherms of ScFe<sub>6</sub>Ge<sub>4</sub> measured at 3, 300, 400, 500 and 600 K. A linear field dependency of the magnetization isotherms above the ordering temperature (500 and 600 K) is expected due to the expected paramagnetic character of the compound. However, at low magnetic fields a steep increase is observed which is most likely due to elementary  $\alpha$ -Fe that exhibits a ferromagnetic ordering at  $T_C = 1041$  K [43]. Nevertheless, the intrinsic ferromagnetic character of ScFe<sub>6</sub>Ge<sub>4</sub> is undoubtedly due to significant steeper increase at low magnetic fields of the 400 K isotherm in comparison to the 500 K one. The magnetic moment at 3

K and 80 kOe is  $0.12(1) \mu_B / \text{Fe atom}$  which is significantly lower than the theoretical saturation magnetizations of  $\text{Fe}^{2+}$  or  $\text{Fe}^{3+}$ .

The discrepancy between calculated and measured moments can be assigned to the fact that the calculations account for a perfect defect void structure, while the measured sample is polycrystalline with a distribution of domain sizes. Ultrafine particles with size below single (mono)-magnetic domain might even be super-paramagnetic.

### 3.5. $^{57}\text{Fe}$ Mössbauer of $\text{ScFe}_6\text{Ge}_4$

The  $^{57}\text{Fe}$  spectrum of  $\text{ScFe}_6\text{Ge}_4$  is presented in Fig. 7 together with a transmission integral fit. It could be well reproduced by a single signal with an isomer shift of  $0.22(1)$  and an experimental line width of  $0.29(1) \text{ mm}\cdot\text{s}^{-1}$  ranging in the usual isomer shift region of metallic iron [44] and intermetallic scandium iron germanides [45]. No second resonance as expected for an  $\alpha\text{-Fe}$  impurity ( $\delta = -0.1 \text{ mm}\cdot\text{s}^{-1}$ ,  $B_{\text{HF}} = 33 \text{ T}$ ) could be observed. A weak quadrupole splitting ( $\Delta E_Q = 0.34(1) \text{ mm}\cdot\text{s}^{-1}$ ) is a consequence of the non-cubic site symmetry of the iron atom. Since the measured spectrum was recorded well below the ferromagnetic ordering temperature a clear Zeeman splitting came visible with a magnetic hyperfine field of  $19.1(1) \text{ T}$ . In order to check the magnetic stability of  $\text{ScFe}_6\text{Ge}_4$  at room temperature a second spectrum was recorded at  $5 \text{ K}$  (not shown here). It lead to the same hyperfine field strength, no increase could be detected.

## Conclusions

Comparative studies with DFT of the electronic and magnetic structures as well as the bonding behavior were carried out for the  $A\text{Fe}_6\text{Ge}_4$  family and comparisons with  $\text{LuTi}_6\text{Sn}_4$  were established. Whereas similar electronic structure trends were observed within the  $A\text{Fe}_6\text{Ge}_4$  family ( $A = \text{Li, Mg, Sc, Zr}$ ) for cohesive energies and the small charge transfer within the Fe substructure, larger electron transfer from the Ti substructure is found. The Fe Kagomé substructure is found magnetically unstable in a spin degenerate configuration and develops finite magnetization with  $M(\text{Fe}) \sim 1.7 \mu_B$  with a spin dependent bonding mainly driven by differentiated COOP( $\uparrow$ ) and COOP( $\downarrow$ ).  $^{57}\text{Fe}$  Mössbauer spectroscopic measurements confirm the metallic character of the Fe atoms predicted by VASP calculations. The ferromagnetic nature of  $\text{ScFe}_6\text{Ge}_4$  is reflected in the magnetic data ( $T_C = 491(3) \text{ K}$ ) as well as in a magnetic hyperfine field splitting of  $19.1 \text{ T}$ .

## Acknowledgments

This work was financially supported by the Deutsche Forschungsgemeinschaft. Computational facilities provided by the MCIA-University of Bordeaux and support from *Conseil Régional d'Aquitaine* are acknowledged. B.G. and O.N. are indebted to the Fonds der Chemischen Industrie and the NRW Forschungsschule *Molecules and Materials – A Common Design Principle* for PhD fellowships.

## References

- [1] F. Laves, *Metallwirtschaft* 15 (1936) 840.
- [2] K.A. Gschneidner Jr., V.K. Pecharsky, *Z. Kristallogr.* 221 (2006) 375.
- [3] P. Villars, K. Cenzual, *Pearson's Crystal Data: Crystal Structure Database for Inorganic Compounds* (release 2013/14), ASM International®, Materials Park, Ohio, USA, **2013**.
- [4] E. Parthé, L. Gelato, B. Chabot, M. Penzo, K. Cenzual, R. Gladyshevskii, *TYPIX–Standardized Data and Crystal Chemical Characterization of Inorganic Structure Types*, *Gmelin Handbook of Inorganic and Organometallic Chemistry*, 8th edition, Springer, Berlin (Germany), **1993**.
- [5] R. Pöttgen, *Z. Anorg. Allg. Chem.* 640 (2014) 869.
- [6] S. Blundell, *Magnetism in Condensed Matter*, Oxford Master Series in Condensed Matter Physics, Oxford University Press, Oxford, 2007.
- [7] E. Welk, H.-U. Schuster, *Z. Naturforsch.* 32b (1977) 749.
- [8] K. Cenzual, L.M. Gelato, M. Penzo, E. Parthé, *Z. Kristallogr.* 193 (1990) 217.
- [9] B.Ya. Kotur, *Dr. Sc. Chemistry Thesis*, Lviv State University, Lviv (1995).
- [10] B.Ya. Kotur, *Croatica Chem. Acta* 71 (1998) 635.
- [11] R.R. Olenych, O.I. Bodak, *Tezizy Dokl. Sov. Kristalloghim. Neorg. Koord. Soeden.* (6th) (1992) 204.
- [12] M. Eul, T. Langer, R. Pöttgen, *Intermetallics* 20 (2012) 98.
- [13] Y.V. Fartushna, A.V. Kotko, M.V. Bulanova, *Chem. Met. Alloys* 2 (2009) 83.
- [14] Y. Fartushna, J. Stępeń-Damm, L. Aksel'rud, M. Manyako, B. Belan, M. Bulanova, R. Gladyshevskii, *XI<sup>th</sup> International Conference on Crystal Chemistry of Intermetallic Compounds*, Lviv (Ukraine), May 30 – June 2 (2010) P24.
- [15] J. Ma, Y. Zhan, J. She, Z. Yang, J. Liang, *J. Alloys Compd.* 489 (2010) 384.
- [16] S.F. Matar, R. Pöttgen, *Z. Anorg. Allg. Chem.* 640 (2014) 1641.
- [17] S.F. Matar, B. Chevalier, R. Pöttgen, *Solid State Sci.* 27 (2014) 5.
- [18] R. Pöttgen, T. Gulden, A. Simon, *GIT Labor-Fachzeitschrift* 43 (1999) 133.
- [19] K. Yvon, W. Jeitschko, E. Parthé, *J. Appl. Crystallogr.* 10 (1977) 73.
- [20] P. Hohenberg, W. Kohn, *Phys. Rev.* 136 (1964) B864.



- [21] W. Kohn, L.J. Sham, *Phys. Rev.* 140 (1965) A1133.
- [22] G. Kresse, J. Furthmüller, *Phys. Rev. B* 54 (1996) 11169.
- [23] G. Kresse, J. Joubert, *Phys. Rev. B* 59 (1999) 1758.
- [24] WEB link: <http://cms.mpi.univie.ac.at/vasp>
- [25] P.E. Blöchl, *Phys. Rev. B* 49 (1994) 17953.
- [26] J.P. Perdew, K. Burke, M. Ernzerhof, *Phys. Rev. Lett.* 77 (1996) 3865.
- [27] D.M. Ceperley, B.J. Alder, *Phys. Rev. Lett.* 45 (1980) 566.
- [28] W.H. Press, B.P. Flannery, S.A. Teukolsky, W.T. Vetterling, *Numerical Recipes*, Cambridge University Press, New York, 1986.
- [29] P.E. Blöchl, *Phys. Rev. B* 49 (1994) 16223.
- [30] M. Methfessel, A.T. Paxton, *Phys. Rev. B* 40 (1989) 3616.
- [31] A.R. Williams, J. Kübler, C.D. Gelatt Jr., *Phys. Rev. B* 19 (1979) 6094.
- [32] V. Eyert, *The Augmented Spherical Wave Method – A Comprehensive Treatment*, Lecture Notes in Physics, Springer, Heidelberg (2007).
- [33] R. Hoffmann, *Angew. Chem. Int. Ed. Engl.* 26 (1987) 846.
- [34] R.A. Brand, Normos Mössbauer fitting Program, Universität Duisburg, Duisburg (Germany), 2007.
- [35] G.M. Sheldrick, *Acta Crystallogr. A* 64 (2008) 112.
- [36] J. Emsley, *The Elements*, Oxford University Press (1999).
- [37] J. Donohue, *The Structures of the Elements*, Wiley, New York (1974).
- [38] H.J. Wallbaum, *Z. Metallkd.* 35 (1943) 218.
- [39] B. Malaman, A. Courtois, J. Protas, B. Roques, *C.R. Séances, Acad. Sci., Sér. C* 276 (1973) 665.
- [40] R.F.W. Bader, *Chem. Rev.* 91 (1991) 893.
- [41] P. Mohn, *Magnetism in the solid state – An introduction*, springer series, in: *Solid-State Sciences*. Springer, Heidelberg, 2003.
- [42] J.F. Janak, *Phys. Rev. B* 16 (1977) 255.
- [43] A.F. Holleman, E. Wiberg, N. Wiberg, *Lehrbuch der Anorganischen Chemie*, Walter de Gruyter, Berlin, 1995.
- [44] A.M. van der Kraan, K.H.J. Buschow, *Physica B+C* 138 (1986) 55.
- [45] T. Mazet, O. Isnard, B. Malaman, *Solid State Comm.* 114 (2000) 91.

Table 1

Lattice parameters of  $\text{LiFe}_6\text{Ge}_4$  type compounds.

Compound	$a$ / pm	$c$ / pm	$V$ / nm <sup>3</sup>	reference
$\text{LiFe}_6\text{Ge}_4$	504.5	1966	0.4334	[7, 8]
$\text{ScFe}_6\text{Ge}_4$	507.9(3)	2000.9(1)	0.4470	this work
$\text{ScFe}_6\text{Ge}_4$	506.6	2001.3	0.4448	[9, 10]
$\text{ZrFe}_6\text{Ge}_4$	507.3(2)	2009.9(9)	0.4480	[11]
$\text{YTi}_6\text{Sn}_4$	578.2(1)	2273.0(5)	0.6582	[12]
$\text{GdTi}_6\text{Sn}_4$	578.6	2279.8	0.6610	[15]
$\text{GdTi}_6\text{Sn}_4$	578.1(2)	2276.1(6)	0.6587	[12]
$\text{TbTi}_6\text{Sn}_4$	577.7(1)	2274.8(2)	0.6575	[12]
$\text{DyTi}_6\text{Sn}_4$	577.2(1)	2268.6(4)	0.6545	[13, 14]
$\text{DyTi}_6\text{Sn}_4$	577.6(1)	2272.1(4)	0.6564	[12]
$\text{HoTi}_6\text{Sn}_4$	577.7(1)	2267.1(4)	0.6553	[12]
$\text{ErTi}_6\text{Sn}_4$	577.1(1)	2266.0(3)	0.6536	[12]
$\text{TmTi}_6\text{Sn}_4$	576.8(1)	2263.7(3)	0.6522	[12]
$\text{LuTi}_6\text{Sn}_4$	577.0(2)	2260.4(5)	0.6517	[12]

Table 2

Crystal data and structure refinement for ScFe<sub>6</sub>Ge<sub>4</sub>, space group  $R\bar{3}m$ ,  $Z = 3$ , Pearson symbol hR33.

Empirical formula	ScFe <sub>6</sub> Ge <sub>4</sub>
Formula weight (g·mol <sup>-1</sup> )	670.42
Lattice parameters	Table 1
Calculated density (g·cm <sup>-3</sup> )	7.47
Crystal size (μm <sup>3</sup> )	10 × 25 × 50
Transm. ratio (max/min)	1.83
Detector distance (mm)	40
Exposure time (sec)	48
$\omega$ range; increment (°)	0–180 / 0.25
Integr. param. (A, B, EMS)	6.4, –8.3, 0.040
Absorption coefficient (mm <sup>-1</sup> )	34.9
$F(000)$	915
$\theta$ range for data collection (°)	3–33
Range in $hkl$	$\pm 7, \pm 7, \pm 30$
Total no. reflections	4911
Independent reflections / $R_{int}$	242 / 0.0610
Reflections with $I \geq 2\sigma(I)$ / $R_{\sigma}$	202 / 0.0200
Data / parameters	242 / 16
Goodness-of-fit on $F^2$	1.057
$R1$ / $wR2$ for $I > 2\sigma(I)$	0.0273 / 0.0720
$R1$ / $wR2$ (all data)	0.0334 / 0.0737
Extinction coefficient	0.0028(5)
Largest diff. peak / hole (e / Å <sup>3</sup> )	1.59 / –1.27

Table 3

Atomic coordinates and anisotropic displacement parameters (pm<sup>2</sup>) for ScFe<sub>6</sub>Ge<sub>4</sub>. The anisotropic displacement factor exponent takes the form:  $-2\pi^2[(ha^*)^2U_{11} + \dots + 2hka^*b^*U_{12}]$ .  $U_{eq}$  is defined as one third of the trace of the orthogonalized  $U_{ij}$  tensor.

Atom	site	$x$	$y$	$z$	$U_{11} = U_{22}$	$U_{33}$	$U_{13} = U_{23}$	$U_{12}$	$U_{eq}$
Sc	3a	0	0	0	185(6)	152(10)	0	93(3)	174(5)
Fe	18h	0.49633(8)	$-x$	0.10182(3)	171(3)	180(4)	7(1)	90(3)	172(3)
Ge1	6c	0	0	0.13226(5)	184(3)	152(4)	0	92(2)	173(3)
Ge2	6c	0	0	0.33256(5)	181(3)	151(5)	0	91(2)	171(3)

Table 4

Interatomic distances (pm) in the structure of  $RFe_6Ge_4$  ( $R = Li, Sc, Zr$ ) and  $LuTi_6Sn_4$ . All distances of the first coordination shells are listed. Standard deviations are all less or equal 0.2 pm.

<b>LiFe<sub>6</sub>Ge<sub>4</sub></b>			<b>ScFe<sub>6</sub>Ge<sub>4</sub></b>			<b>ZrFe<sub>6</sub>Ge<sub>4</sub></b>			<b>LuTi<sub>6</sub>Sn<sub>4</sub></b>						
Li:	2	Ge1	247.7	Sc:	2	Ge1	264.6	Zr:	2	Ge1	267.5	Lu:	2	Sn1	286.2
	6	Ge2	291.3		6	Ge2	293.2		6	Ge2	292.9		6	Sn2	333.1
	12	Fe	323.5		12	Fe	325.6		12	Fe	326.7		12	Ti	374.7
Fe:	1	Ge2	248.9	Fe:	2	Fe	248.4	Fe:	1	Ge1	241.6	Ti:	2	Ti	281.8
	1	Ge2	250.0		1	Ge1	248.8		2	Fe	243.0		1	Sn1	284.8
	1	Ge1	251.6		1	Ge2	250.4		1	Ge2	248.5		1	Sn2	291.0
	2	Fe	252.3		1	Ge2	251.7		1	Ge2	256.8		1	Sn2	291.8
	2	Fe	252.3		2	Fe	259.5		2	Ge1	261.1		2	Sn1	292.3
	2	Ge1	256.3		2	Ge1	261.2		2	Fe	264.3		2	Ti	295.2
	2	Fe	289.6		2	Fe	296.5		2	Fe	300.0		2	Ti	319.8
	2	Li	323.5		2	Sc	325.6		2	Zr	326.7		2	Lu	374.7
Ge1:	1	Li	247.7	Ge1:	3	Fe	248.8	Ge1:	3	Fe	241.6	Sn1:	3	Ti	284.8
	3	Fe	251.6		6	Fe	261.2		6	Fe	261.1		1	Lu	286.2
	6	Fe	256.3		1	Sc	264.6		1	Zr	267.5		6	Ti	292.3
Ge2:	3	Fe	248.9	Ge2:	3	Fe	250.4	Ge2:	3	Fe	248.5	Sn2:	3	Ti	291.0
	3	Fe	250.0		3	Fe	251.7		3	Fe	256.8		3	Ti	291.8
	3	Li	291.3		3	Sc	293.2		3	Zr	292.9		3	Lu	333.1
	3	Ge2	291.3		3	Ge2	293.2		3	Ge2	292.9		3	Sn2	333.1

Table 5

Geometry optimized lattice parameters and atomic coordinates of  $ScFe_6Ge_4$  and predicted  $MgFe_6Ge_4$

Atom	site	$x$	$y$	$z$
<b>ScFe<sub>6</sub>Ge<sub>4</sub> (<math>a = 507</math> and <math>c = 2008</math> pm)</b>				
Sc	$3a$	0	0	0
Fe	$18h$	0.496	$-x$	0.102
Ge1	$6c$	0	0	0.132
Ge2	$6c$	0	0	0.333
<b>MgFe<sub>6</sub>Ge<sub>4</sub> (<math>a = 509</math> and <math>c = 2010</math> pm)</b>				
Mg	$3a$	0	0	0
Fe	$18h$	0.481	$-x$	0.100
Ge1	$6c$	0	0	0.133
Ge2	$6c$	0	0	0.331

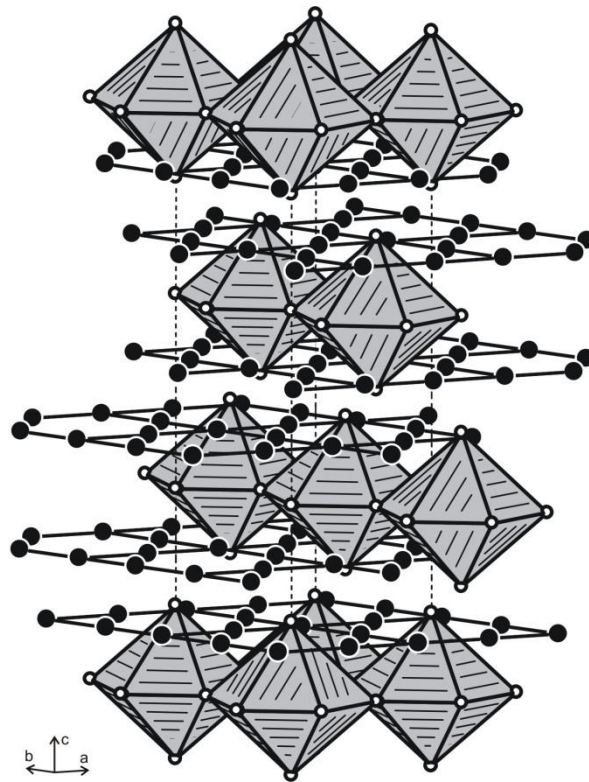


**Fig. 1.** Crystal structure of ScFe<sub>6</sub>Ge<sub>4</sub>. The iron Kagomé networks and the edge-sharing Sc@Ge<sub>8</sub> hexagonal bipyramids are emphasized.

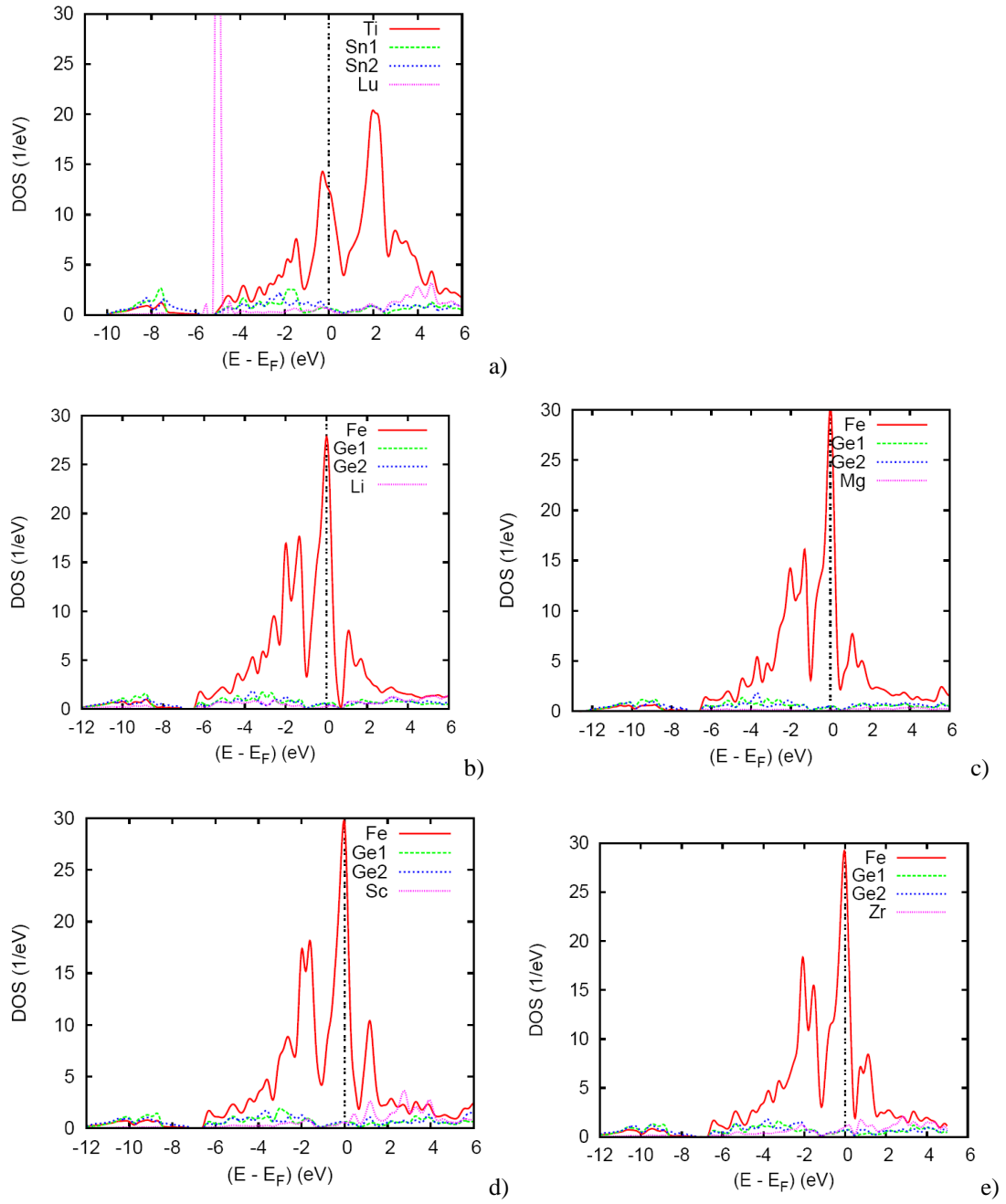


**Fig. 2.** Site projected DOS (PDOS) for the  $A\text{Fe}_6\text{Ge}_4$  ( $A = \text{Li}, \text{Mg}, \text{Sc}, \text{Zr}$ ) series and  $\text{LuTi}_6\text{Sn}_4$  under inspection in spin degenerate NSP configuration.

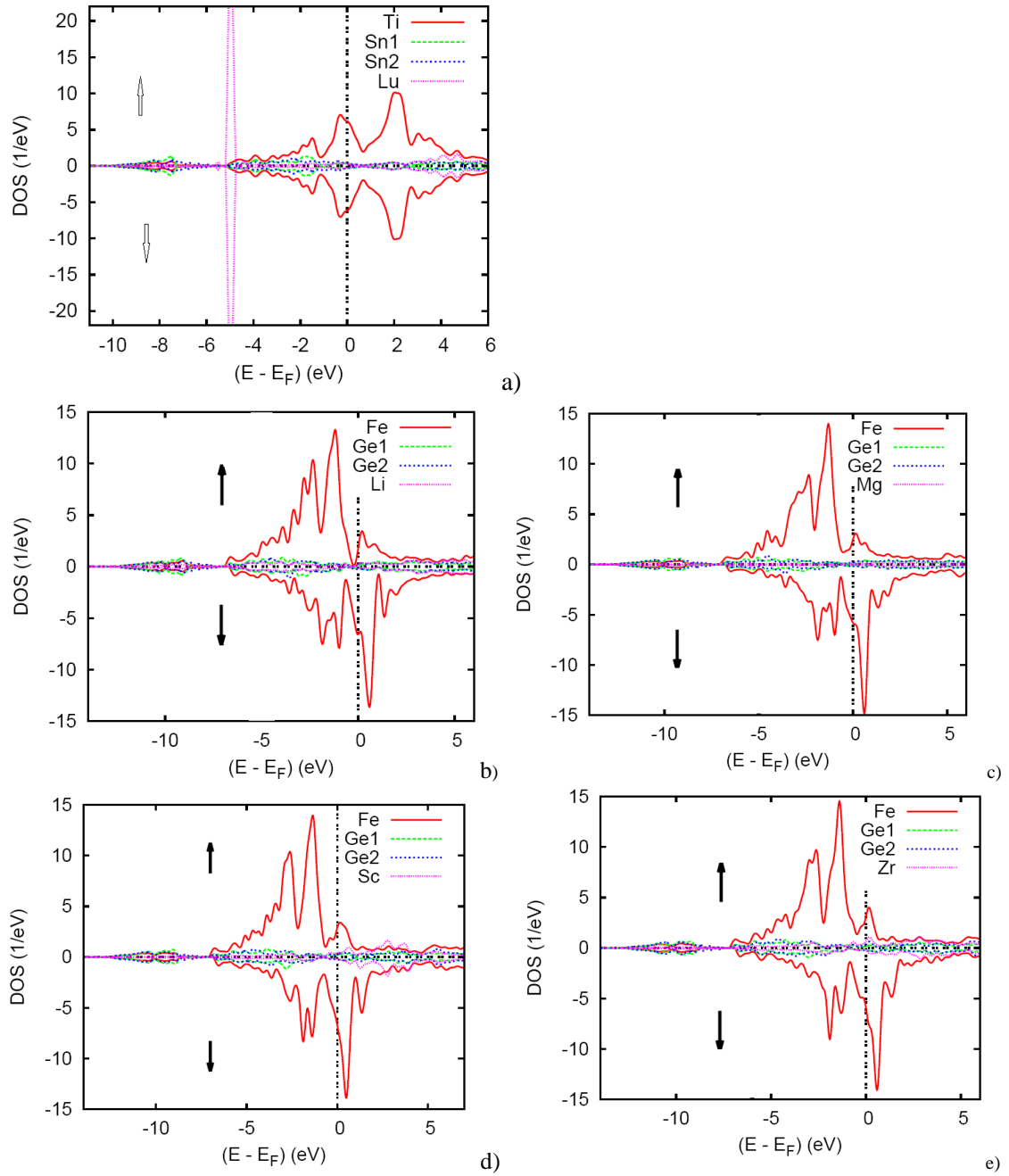


**Fig. 3.** Site and spin projected DOS for the  $A\text{Fe}_6\text{Ge}_4$  ( $A = \text{Li}, \text{Mg}, \text{Sc}, \text{Zr}$ ) series and  $\text{LuTi}_6\text{Sn}_4$  in spin polarized SP configuration.

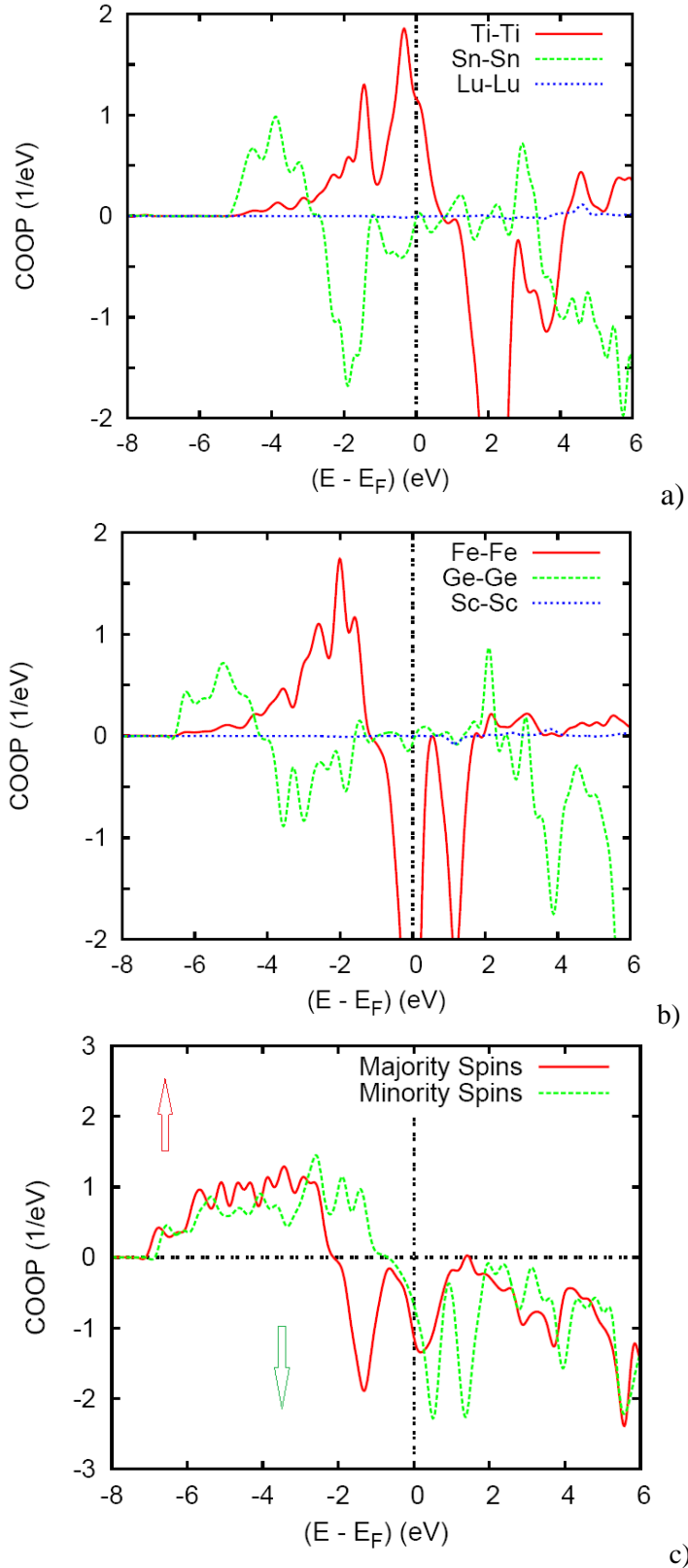


**Fig. 4.** Chemical bonding between substructures of the same kind in a) LuTi<sub>6</sub>Sn<sub>4</sub>, b) ScFe<sub>6</sub>Ge<sub>4</sub>, and c) SP ScFe<sub>6</sub>Ge<sub>4</sub> for total  $\uparrow$  (majority spins) and  $\downarrow$  (minority spins) projected COOP.



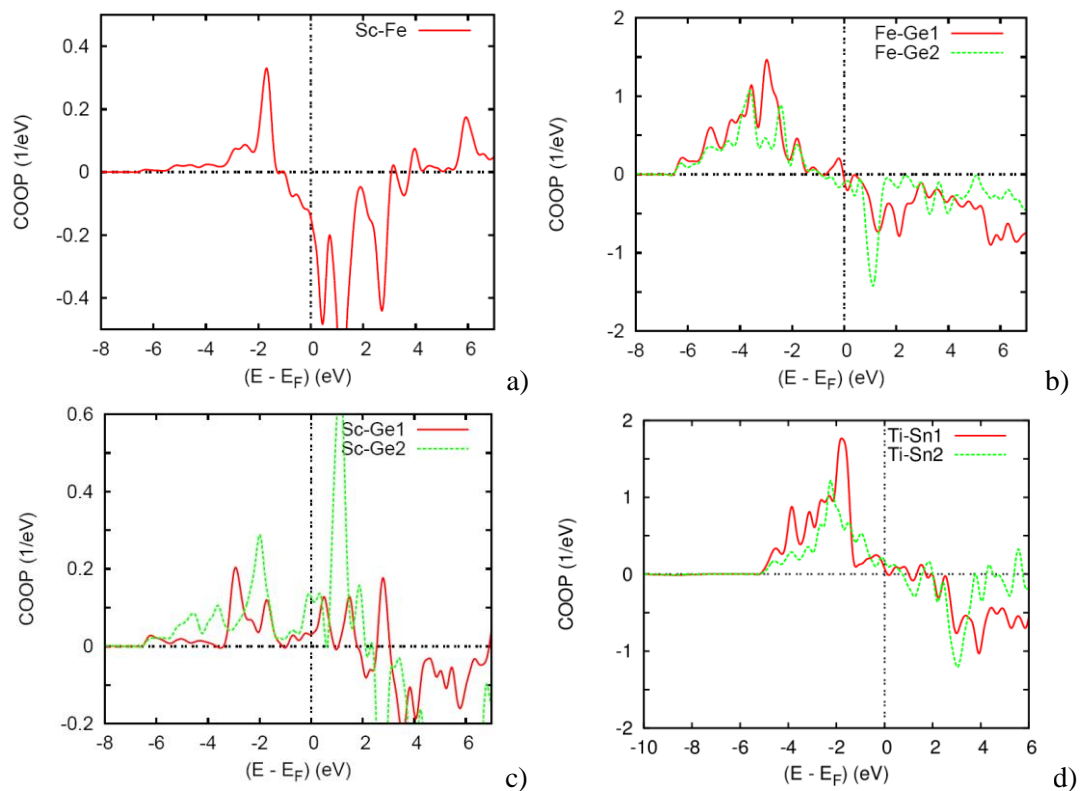


**Fig. 5.**  $\text{ScFe}_6\text{Ge}_4$ : Chemical bonding for the Sc-Fe (a), Fe-Ge (b) and Sc-Ge (c) at Ge1 and Ge2 substructures. Panel d) shows the Ti-Sn COOP in  $\text{LuTi}_6\text{Sn}_4$  for comparison (see text).

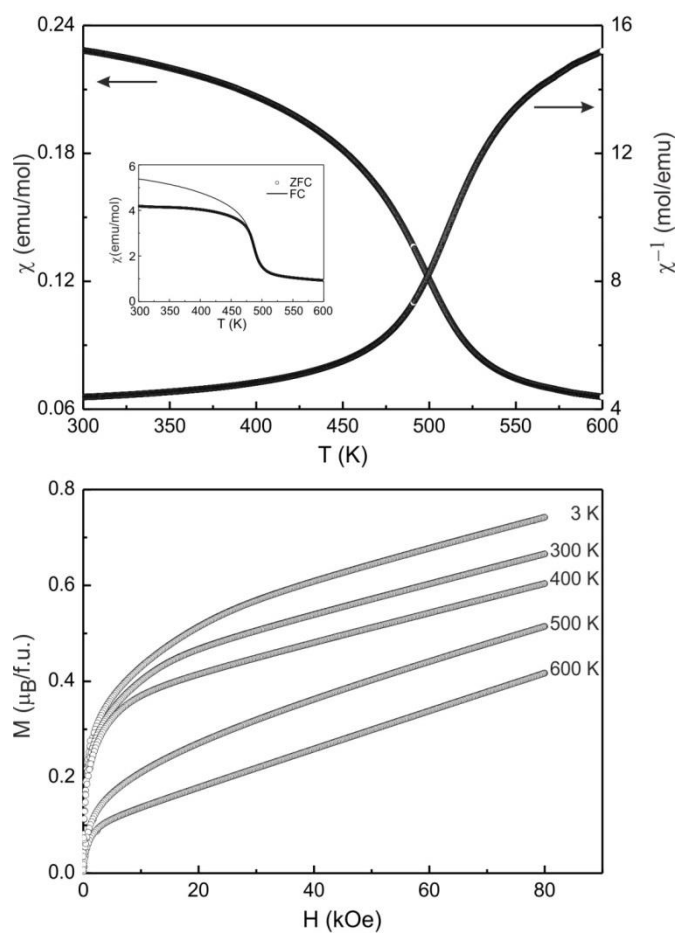


**Fig. 6.** Magnetic properties of  $\text{ScFe}_6\text{Ge}_4$ : (top) Temperature dependence of the magnetic susceptibility  $\chi$  and its reciprocal  $\chi^{-1}$  in the range of 300 to 600 K measured with a magnetic field strength of 10 kOe. The inset shows the magnetic susceptibility in zero-field- (ZFC) and field-cooled (FC) mode at 100 Oe; (bottom) Magnetization isotherms at 3, 300, 400, 500 and 600 K.

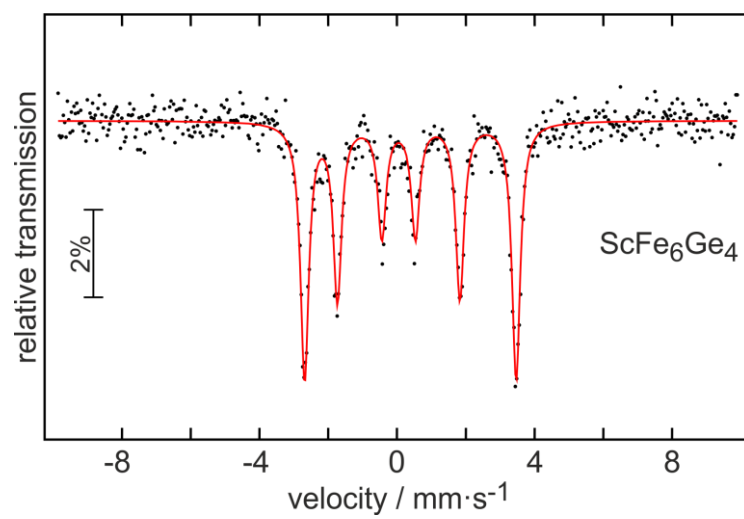


**Fig. 7.** Experimental (data points) and simulated (continuous lines) <sup>57</sup>Fe Mössbauer spectra at ambient temperature.